



Au(I)-based compounds inhibit nsp14/nsp10 and nsp13 (helicase) to exert anti-SARS-CoV-2 properties

Jingxin Chen^{1,2} · Xueying Wei^{1,2} · Chun-Lung Chan¹ · Kaiming Tang² · Shuofeng Yuan² · Hongyan Li¹ · Hongzhe Sun¹

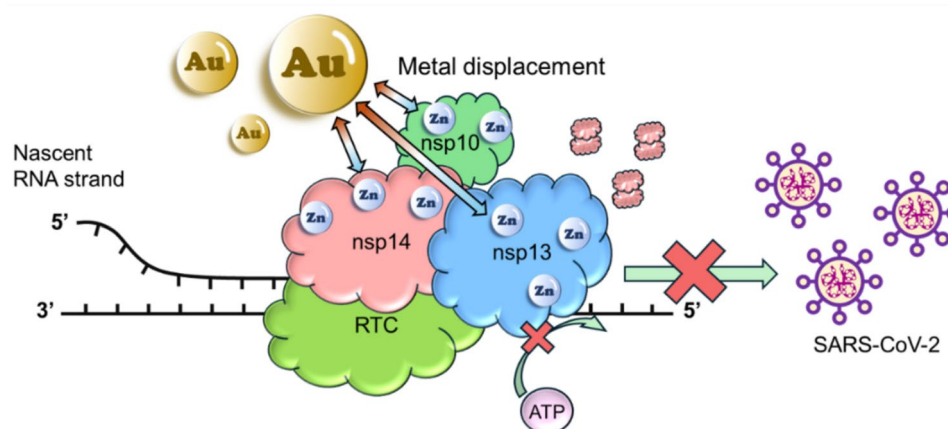
Received: 24 March 2025 / Accepted: 3 June 2025 / Published online: 18 June 2025

© The Author(s) 2025

Abstract

Au(I) compounds have long been associated with medicine for the treatment of various diseases, especially auranofin has been used for the treatment of rheumatoid arthritis. In addition, Au(I) based compounds also exhibit anti-cancer, anti-bacteria properties. The recent prevalence of the COVID-19 pandemic, caused by severe acute respiratory syndrome coronavirus 2 (SARS-CoV-2), has aroused attention to investigate the antiviral potential of Au(I) compounds. Herein we demonstrate the pan-anti-SARS-CoV-2 activity of Au(I) metallodrugs in mammalian cells. We synthesized a panel of Au(I)-based compounds and found that these compounds could effectively inhibit the exoribonuclease and methyltransferase activities of SARS-CoV-2 nsp14/nsp10 complex, and the ATPase and DNA unwinding activities of SARS-CoV-2 nsp13 (helicase). Mechanistic studies reveal that Au(I) can not only displace the critical Zn(II) ions from nsp14/nsp10 complex and nsp13 but also changes the secondary and quaternary structure of nsp14 and perturbate the DNA unwinding of nsp13 by disrupting the ATP binding. This study illustrates a multi-target feature Au(I) compounds/drug agents for the viruses, highlighting their potential as pan-anti-SARS-CoV-2 (or relevant viruses) agents.

Graphical Abstract



Keywords SARS-CoV-2 · Antiviral · Metallodrug · nsp14 · Helicase · Gold

Introduction

The COVID-19 disease, caused by severe acute respiratory syndrome coronavirus 2 (SARS-CoV-2), has posed huge health challenges and economic loss worldwide. Although effective vaccines have been made to provide prophylactic protection for healthy adults, a large population with

Jingxin Chen and Xueying Wei contribute equally to this work.

Extended author information available on the last page of the article

compromised immune systems or underlying medical conditions remains unvaccinated and the emergence of viral variants as well as immune escape mutation in the spike (S) protein also reduces vaccine effectiveness. Thus, developing potent broad-spectrum antivirals against SARS-CoV-2 and its variants is an imperative safeguard against future outbreaks and pandemics.

Upon cellular entry, SARS-CoV-2 genome encodes 16 nonstructural proteins (nsps), playing vital roles during viral transcription and replication in the host [1]. Some of these proteins have been shown to serve as druggable targets. For example, nsp3 and nsp5, which are papain-like protease (PLpro) and 3-chymotrypsin-like protease (3CLpro or Mpro) respectively, are the two mostly investigated anti-viral targets for SARS-CoV-2 and over 50 non-covalent and covalent inhibitors including GRL0617 analogues, have been reported [2]. Besides, 3CLpro inhibitors including Lopinavir, Ritonavir, Danoprevir, PF07321332 in combination with Ritonavir (Paxlovid®), ASC09F in combination with Oseltamivir, Darunavir in combination with Cobiscistat, and the noncovalent inhibitor S-217622 and Atazanavir are currently being investigated in clinical trial [3–10]. However, no rationally designed drug-like PLpro inhibitors display both in vitro and in vivo antiviral activity against both SARS-CoV-2 and MERS-CoV infection attributable to the structure differences between MERS-PLpro and SARS-PLpro. Besides, multiple mutations have been identified in Mpro among the SARS-CoV-2 and resistance to Mpro inhibitors is expected to rise with the increasing prescription [11, 12]. In addition, as Ritonavir is a potent inhibitor of the CYP3A4 isoenzyme, target selectivity and drug–drug interactions should also be taken into consideration [13]. As such, broad-spectrum antiviral strategies targeting the conserved elements of the virus replication cycle are needed to combat emerging variants and drug-resistant viruses. We anticipate that nsp14/nsp10 complex and nsp13 (helicase) stand out as two very promising targets for this purpose.

SARS-CoV-2 nsp14 functions both as an exoribonuclease together with its critical cofactor nsp10 and as a S-adenosyl methionine-dependent (guanine-N7) methyltransferase (MTase) [14]. The N-terminal ExoN domain of nsp14 plays a critical excision role in improving RNA synthesis fidelity to prevent lethal mutagenesis by removing mismatched nucleotides or nucleotide analogs from the virus ssRNA in a 3' to 5' direction [15]. The C-terminal domain of nsp14 displays N7-guanine MTase activity to assemble the cap structure at the 5' end of the virus mRNA [16]. In SARS-CoV-2 nsp14/nsp10 complex, nsp10 is a critical cofactor of nsp14 which facilitates the formation of the ExoN active site, thus significantly stimulating the ExoN activity of nsp14 [17]. SARS-CoV-2 nsp13 plays an important role in helicase (nucleoside triphosphate enzymes (NTPs)) in viral replication. Nsp13 is an RNA 5'-triphosphatase and the

hydrolysis of NTPs provides energy for its RNA or DNA duplexes unwinding activity with 5'-3' directionality [18]. Sequence analysis shows that both nsp14/nsp10 complex and nsp13 are highly conserved among closely related coronavirus species, i.e., SAR-CoV-1 and MERS-CoV (Fig. S1). It is more noteworthy that nsp14/nsp10 complex and nsp13 contain five (three in nsp14 and two in nsp10) and three highly conserved zinc-binding sites, all of which play indispensable roles in enzyme activity [19, 20]. Therefore, combined with their critical functions in the viral life cycle, targeting these zinc-binding sites of nsp14/nsp10 complex and nsp13 may serve as a good strategy for the development of broad-spectrum anti-SARS-CoV-2 drugs [19, 21].

Metal-based strategy has been shown promising in combating COVID-19 [22]. Indeed, we have shown that bismuth-based drugs and compounds exhibit excellent activity against SARS-CoV-2 both in infected cells and in animal models [20, 23]. Mechanistic studies show that bismuth targets both nsp14/nsp10 and nsp13 in cells, leading to inactivating of the enzymatic activity owing to the displacement of zinc [19, 21]. In addition, a gold-based drug, auranofin, was proposed to be a promising drug against SARS-CoV-2 infection in early 2020 and soon thereafter, it was demonstrated to inhibit replication of SARS-CoV-2 in human cells at low micromolar concentration and significantly reduce the expression of cytokines induced by virus infection [24, 25]. Furthermore, oral administration of auranofin to Syrian hamsters reduced viral replication, IL-6 production, and inflammation in lungs in both therapeutic and prophylactic regimens [26]. Au(I) compounds were also shown to inhibit spike-ACE2 interaction and SARS-CoV-2 PLpro activity, thus serving as potential antivirals [27, 28]. Mechanism of Au(I) compounds against PLpro activity was also correlated to their ability to remove essential zinc ions from the enzyme [28]. As zinc fingers usually play important structural or catalytic roles in the proteins, such ejection of Zn ions from the key enzymes of SAR-CoV-2 was previously reported to be a potent strategy of clinically safe Zn-ejector drugs, disulfiram and ebselen, against virus infection [29]. Besides, it was also found that auranofin and its halido analogues as well as gold carbene complexes can inhibit SARS-CoV-2 Mpro activity, which may be related to its binding to functionally relevant cysteine residues of the protein [30]. In fact, auranofin was one of the first metallodrugs to show potential antiviral activity. A patient with human immunodeficiency virus (HIV) infection and disabling psoriatic arthritis showed improved CD4 counts and drastically reduced opportunistic infections upon auranofin treatment [31]. Following that, more and more antiviral studies were conducted on gold metallodrugs against other viral diseases including Chikungunya virus (CHIKV) and the flavivirus Zika virus [32]. Given that Au(I), a soft metal prefers to bind to enzymes containing accessible and functionally important

thiol groups, zinc-binding sites of nsp14/nsp10 complex and nsp13 make them potential targets of Au(I) metallodrugs.

Herein, we showed that Au(I) metallodrugs exhibited effective anti-SARS-CoV-2 activity against both BA.5.2 and XBB strains in infected mammalian cells. Based on enzymatic studies, we found that Au(I) metallodrugs could significantly inhibit both the ExoN and MTase activities of nsp14/nsp10 complex and the ATPase and DNA unwinding activities of nsp13. Further mechanistic studies reveal that Au(I) metallodrugs could exert their anti-SARS-CoV-2 activity through displacing Zn(II) from the zinc-finger sites of nsp14/nsp10 complex and nsp13, leading to protein conformational change of nsp14 and disruption of ATP energy support for DNA unwinding of nsp13. This study highlights the potential of Au(I) metallodrugs as pan-anti-SARS-CoV-2 agents by targeting nsp14/nsp10 complex and nsp13.

Results and discussion

Au(I) metallodrugs inhibit SARS-CoV-2 and its variants in infected mammalian cells

Historically, Au(I) metallodrugs have been used as anti-arthritic drugs, but their antiviral activity has not been extensively explored. Previously it was shown that auranofin could inhibit the SARS-CoV-2 (USA-WA1/2020) in mammalian cells [24], which indicates the potential of Au(I) metallodrugs as anti-SARS-CoV-2 agents. Given the emergence of various SARS-CoV-2 variants, which has developed resistance to many drugs that were effective against early strains, it remains elusive whether Au(I)-based drugs/compounds serve as pan-SARS-CoV-2 agents.

Since auranofin is the only Au(I) metallodrug reported so far to inhibit SARS-CoV-2 infection at the cellular level to date, we chose auranofin as a showcase to examine the pan-anti-SARS-CoV-2 activity of Au(I) metallodrugs. The pan-anti-SARS-CoV-2 potency of Au(I) was evaluated by determining its ability to inhibit viral replication in virus-infected mammalian cells. Firstly, VeroE6-TMPRSS2 cells were infected with SARS-CoV-2 variants with stronger immune escape ability (as Omicron BA.5.2 and XBB), followed by treatment with auranofin at nontoxic concentrations (0–10 μM) for 48 h [20]. Then, the viral load in the cell culture supernatant was assessed by quantitative reverse transcription polymerase chain reaction (RT-qPCR). As shown in Fig. 1, auranofin effectively reduced viral RNA loads in a dose-dependent manner, with the viral load in the cell culture supernatant reduced by a maximum of 4–6 \log_{10} units, demonstrating its good performance in inhibiting these SARS-CoV-2 variants. A plaque reduction assay revealed that auranofin inhibited SARS-CoV-2 virus replication with a half maximal effective concentration (EC_{50}) of $0.73 \pm 0.21 \mu\text{M}$, indicative of auranofin can exert pan-anti-SARS-CoV-2 activity of in mammalian cells.

Au(I) compounds inhibit SARS-CoV-2 nsp14/nsp10 and nsp13 activity in vitro

Due to the thiophilic property of Au(I), the cysteine-rich zinc finger-containing nsp14/nsp10 complex and nsp13 are very likely to be important targets of Au(I) metallodrugs against SARS-CoV-2. To evaluate whether Au(I)-based compounds could inhibit enzymatic activity of nsp14/nsp10 and nsp13, we synthesized 14 Au(I)-based compounds and selected 5 commercially available Au(I) drugs/compounds (i.e., auranofin, Au(PET_3)Cl, gold(I) chloride (AuCl), gold(I)

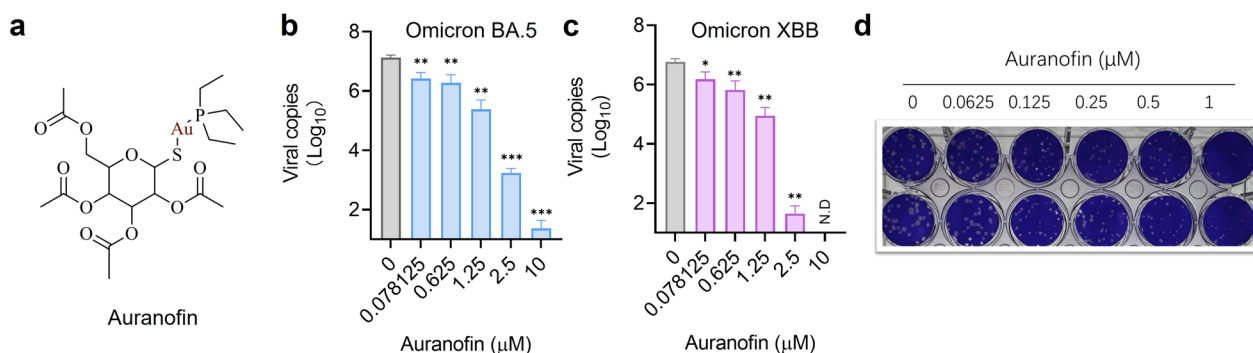


Fig. 1 Pan-anti-SARS-CoV-2 activity of Au(I) metallodrugs in mammalian cells. **a** Structure of auranofin. **b–c** Dose-dependent inhibition of auranofin on replication of SARS-CoV-2 BA.5.2 strain (**b**) and XBB (**c**) in VeroE6-TMPRSS2 cells (MOI=0.01). Viral load in the cell culture supernatant was quantified by qRT-PCR at 48 h.p.i. (hour-post-infection). **d** EC_{50} of auranofin against SARS-CoV-2

determined by plaque reduction assay ($n=2$). For the compounds dissolved in DMSO, the final concentration of DMSO was kept at 1%. Data are shown as mean \pm SD. Statistical significance between the drug treatment group and the vehicle group (0 μM) was determined by an unpaired two-tailed Student's t -test ($n=3$); * $P < 0.05$, ** $P < 0.01$ and *** $P < 0.001$

sodium thiosulfate ($\text{Na}_3\text{Au}(\text{S}_2\text{O}_3)_2$) and sodium aurothiomalate (AuTM) for preliminary screening against SARS-CoV-2 nsp14/nsp10 and nsp13.

Among these compounds, auranofin, an anti-rheumatoid arthritis drug consists of three parts, phosphine, Au(I) and thiolate, in which the top phosphine part and the lower thiolate part can be modified to improve its antiviral activity. For the triethylphosphine moiety, a total of 4 groups were tested including triethylphosphine, trimethylphosphine, urotropine-phosphine and thiophene, and for the bottom thiolate's moieties, different binding motifs such as dithiocarbamate, thiolates and thiourea were tested. These thiourea and selenourea were used which normally give much better solubility as the complexes would become positively charged and have enough stability. Chemical structures of selected compounds are shown in Fig. 2 and detailed synthesis information is shown in supporting information (SI).

For preliminary screening, firstly, we overexpressed and purified nsp10, nsp14 and nsp13 as previously reported [19–21]. We then examined the potential of Au(I)-based compounds/drugs as inhibitors of nsp14/nsp10 and nsp13 by enzymatic activity assays, colloidal bismuth subcitrate

(CBS), a previously reported inhibitor was used as a positive control [19, 20]. For nsp14, the ExoN activity of its complex with nsp10 was detected by a FRET-based exoribonuclease assay, whereas MTase activity was examined by a MTase-Glo methyltransferase assay which monitors the transfer of methyl from SAM to an analog of GpppA-RNA cap structure. For nsp13, ATPase activity was examined by a typical phosphate release assay, in which the phosphate release due to ATP hydrolysis is presented as the relative percentage to evaluate ATPase activity, and its DNA unwinding activity was detected by a FRET-based DNA-duplex unwinding assay [21].

As shown in Fig. 3, the activities of both nsp14 and nsp13 were inhibited to varying degrees upon treatment with 50 mol equiv of Au(I)-based compounds. For both ExoN and MTase activity of nsp14/nsp10 complex, significantly, over 75% of the Au(I)-based compounds showed > 85% inhibition on ExoN activity and over 60% of Au(I)-based compounds showed > 50% inhibition on MTase activity. It is found that the pK_a of the bottom thiolate ligands is correlated to its activity. In general, the higher the pK_a of the thiolates, the better the inhibition. As a result, thiourea-bearing complexes

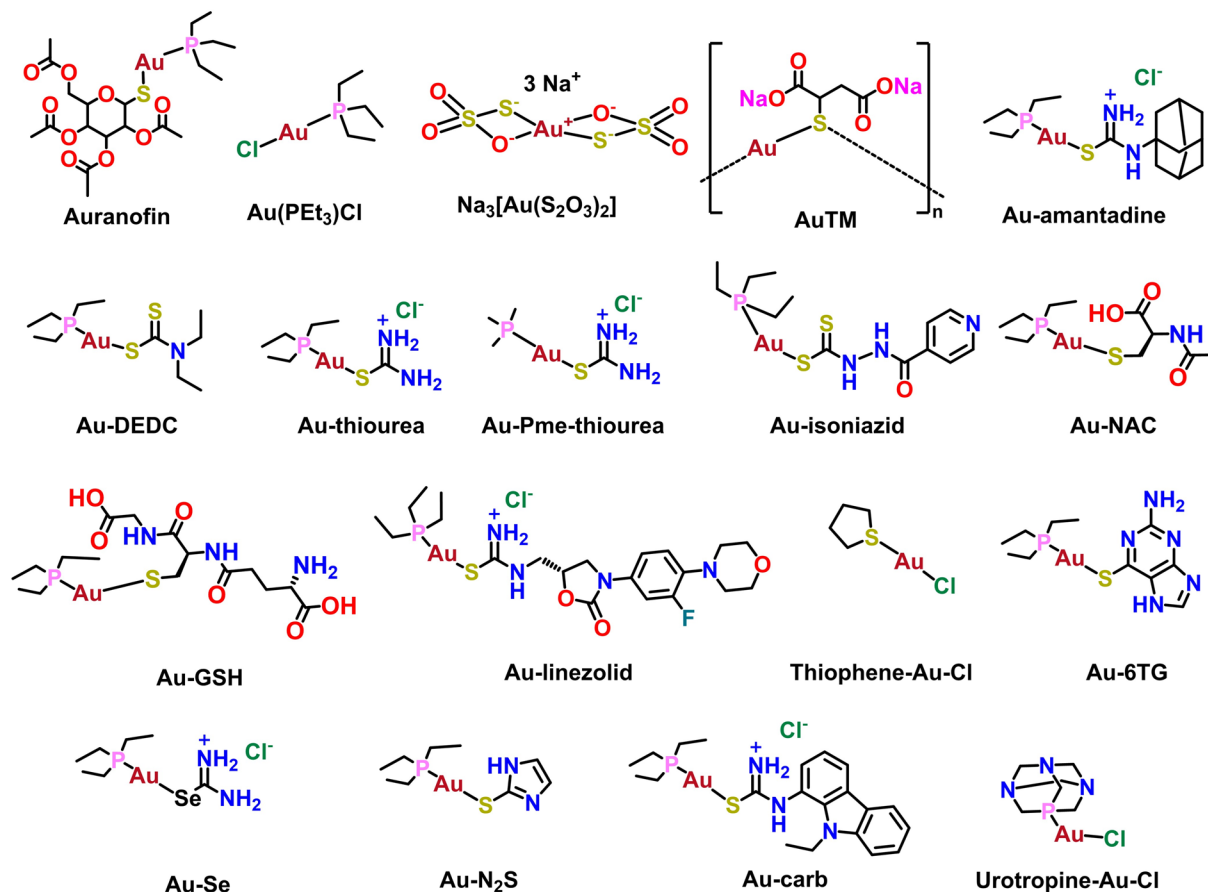


Fig. 2 Chemical structures of selected Au(I)-based drugs/compounds

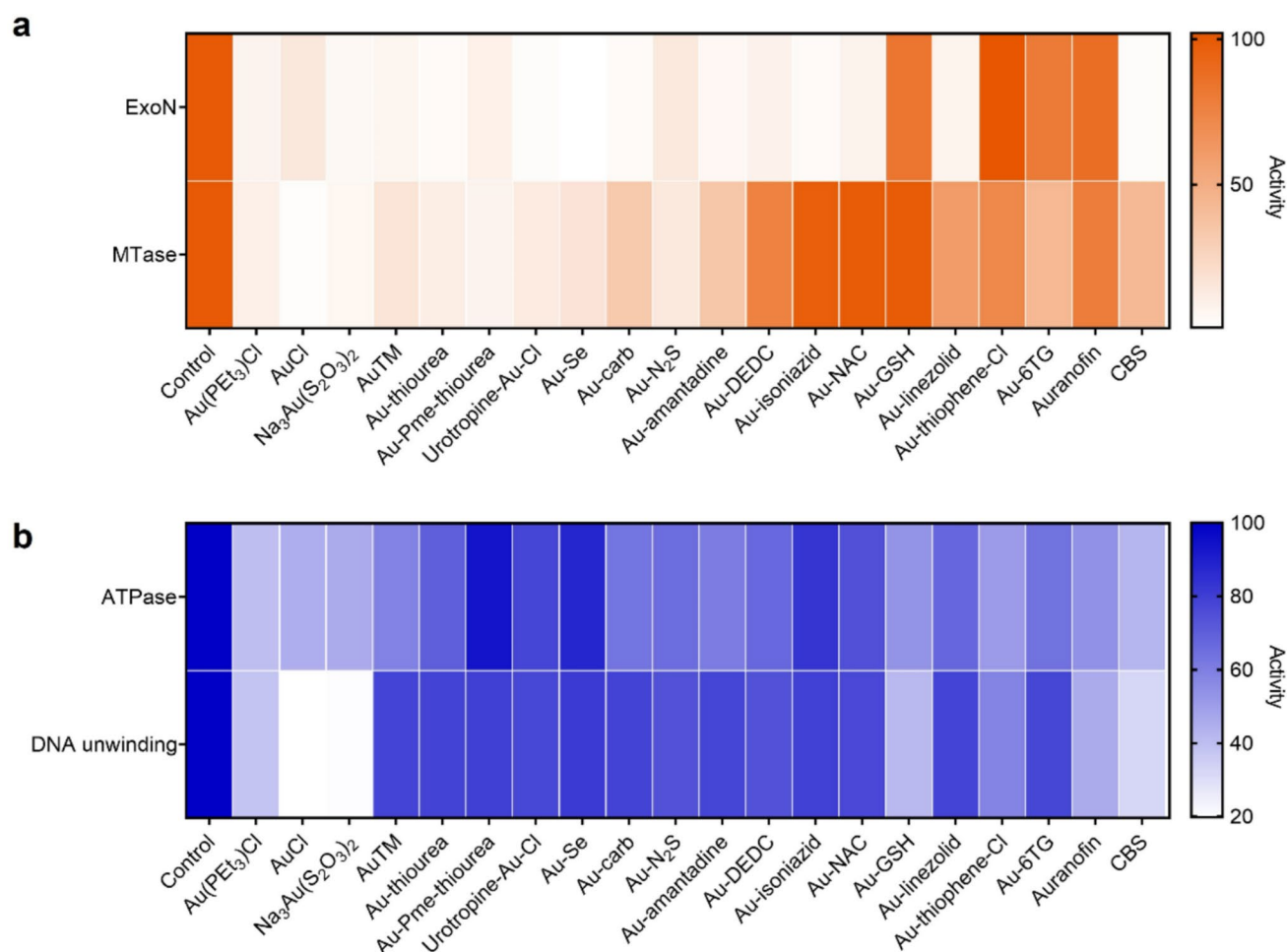


Fig. 3 SARS-CoV-2 nsp14/nsp10 and nsp13 as potential targets of Au(I)-based compounds. ExoN and MTase activities of nsp14 (a) as well as ATPase and DNA unwinding activities of nsp13 (b) in the presence of 50 molar equivalents of Au(I)-based compounds ($n = 3$)

have a much better inhibition than ordinarily thiolates complexes, which also have a lower toxicity. However, the best phosphine groups for both functions are very different. For ExoN activity, urotropine-Au-Cl has excellent inhibition of only 0.68% enzyme activity remaining, which might be due to the electrostatic interaction between aspartate (D211 and D415) around the zinc finger and the positive charge might contribute to strongly binding and better activity, while for MTase, PMe_3 was found to be the best phosphine group.

For both functions of nsp13, $\text{Au}(\text{PET}_3)\text{Cl}$ and other gold salts showed the best results. Among other Au(I)-based compounds, Au-GSH complex also showed good results with 51.33% and 41.67% enzymatic activity remaining for ATPase and DNA unwinding activity respectively. As the zinc finger sites are far away from both active sites, the structure–activity relationship is not obvious due to minimum destruction with most of the complexes showing moderate inhibition (60–80% activity remaining). However, some compounds ($\text{Au}(\text{PET}_3)\text{Cl}$, AuCl, $\text{Na}_3\text{Au}(\text{S}_2\text{O}_3)_2$, etc.) that

exhibited excellent inhibition on nsp14 activities could also inhibit more than 50% of ATPase and DNA unwinding activities of nsp13 simultaneously, revealing a high potential of Au(I)-based compounds as multi-targeted anti-SARS-CoV-2 agents. Based on the inhibition of both nsp14 and nsp13 by $\text{Au}(\text{PET}_3)\text{Cl}$, AuCl, $\text{Na}_3\text{Au}(\text{S}_2\text{O}_3)_2$ and Au-amantadine, these 4 compounds were selected for further evaluation.

As shown in Fig. 4, all these 4 Au(I)-based compounds exhibited dose-dependent inhibition on ExoN and MTase activities of nsp14 as well as ATPase and DNA unwinding activities of nsp13. Importantly, the half-maximum inhibitory concentration (IC_{50}) (Table 1) of $\text{Au}(\text{PET}_3)\text{Cl}$, AuCl, $\text{Na}_3\text{Au}(\text{S}_2\text{O}_3)_2$ and Au-amantadine were determined to be at micromolar level, most of which are lower than $1 \mu\text{M}$. Specifically, the IC_{50} values of $\text{Au}(\text{PET}_3)\text{Cl}$ were as low as $0.38 \pm 0.04 \mu\text{M}$ for nsp14 ExoN activity, and IC_{50} values of AuCl were 0.91 ± 0.01 , 0.20 ± 0.01 and $0.20 \pm 0.03 \mu\text{M}$ for MTase activity of nsp14, ATPase and DNA unwinding activities of nsp13, respectively, indicating the great potentials

Fig. 4 Dose-dependent inhibition of selected Au(I)-based compounds against SARS-CoV-2 nsp14/nsp10 and nsp13. ExoN (**a**) and MTase (**b**) activities of nsp14 as well as ATPase (**c**) and DNA unwinding (**d**) activities of nsp13 were examined in the presence of increasing concentrations of Au(PET₃)Cl, AuCl, Na₃[Au(S₂O₃)₂] and Au-amantadine ($n = 3$). IC₅₀ values are presented as mean values \pm SD in Table 1

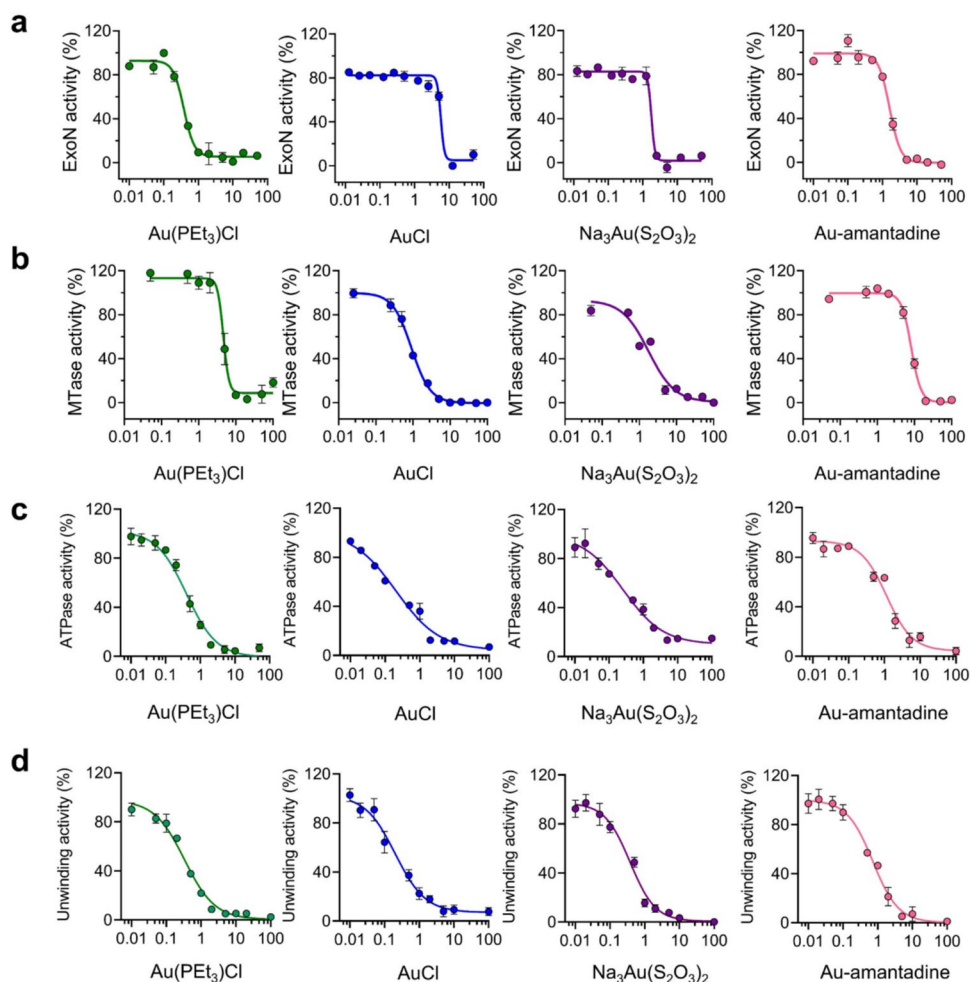


Table 1 IC₅₀ values for selected Au(I)-based compounds against SARS-CoV-2 nsp14/nsp10 and nsp13

Compound	IC ₅₀ (\pm SD) (μ M)			
	ExoN	MTase	ATPase	DNA unwinding
Au(PET ₃)Cl	0.38 \pm 0.04	4.50 \pm 0.98	0.40 \pm 0.09	0.33 \pm 0.04
AuCl	5.78 \pm 0.31	0.91 \pm 0.01	0.20 \pm 0.01	0.20 \pm 0.03
Na ₃ Au(S ₂ O ₃) ₂	1.71 \pm 0.09	1.77 \pm 0.01	0.25 \pm 0.08	0.38 \pm 0.05
Au-amantadine	1.57 \pm 0.12	8.16 \pm 0.18	1.15 \pm 0.23	0.72 \pm 0.13

of Au(I)-based compounds as anti-SARS-CoV-2 drugs by targeting nsp14/nsp10 and nsp13.

Au(I) compounds inhibit nsp14/nsp10 complex by displacing its essential Zn(II)

Next, we explored the inhibition mechanism of nsp14/nsp10 by Au(I). We first investigated the inhibition mode of Au(I) on the dual activities of nsp14, for which we

selected Au(PET₃)Cl as a showcase. To explore the influence of Au(I) on the kinetics of the nsp14/nsp10 ExoN activity, a 20-nucleotide 5'-dU overhang conjugated to a Cy3/BHQ2 pair was used as an RNA duplex substrate. Then, the reciprocals of the reaction velocity and the concentration of the two substrates were used to plot the Lineweaver–Burk plot. And the Michaelis–Menten constant (K_m) and the maximum reaction rate (V_{max}) were calculated by nonlinear fitting to the Michaelis–Menten equation. We found that, in the presence of different molar equivalents of Au(I), K_m values were maintained at 40.4 ± 0.3 nM; whereas V_{max} values decreased from 2.7 to 0.5 nM min⁻¹ (Fig. 5a), suggesting that Au(I) inhibits the ExoN activity of nsp14/nsp10 via a typical noncompetitive mode. The influence of Au(I) on the RNA-binding capability of SARS-CoV-2 nsp14 was also evaluated by an electrophoretic mobility shift assay (EMSA). Our data show that nsp14 led to a significant shift of the dsRNA substrate in the gel, confirming the formation of the nsp14–RNA complex. Supplementation of increasing amounts of Au(I) showed negligible effects on the formation of the protein–RNA complex (Fig. S2), which is consistent with

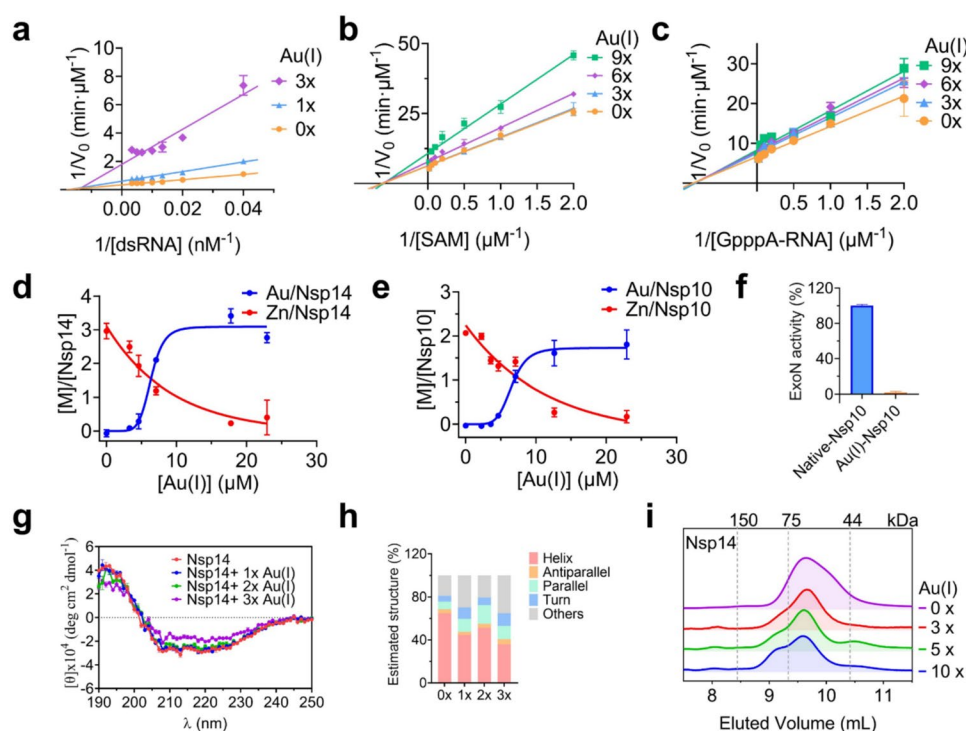


Fig. 5 Au(I) inhibits nsp14/nsp10 complex by displacing its essential Zn(II). **a** Kinetic analysis of nsp14 ExoN activity inhibited by Au(PEt₃)Cl. **b–c** SAM-dependent (**b**) and GpppA-RNA (**c**) kinetic analysis of nsp14 MTase activity inhibited by Au(PEt₃)Cl. **d–e** The substitution of Zn(II) in native nsp14 (**d**) and nsp10 (**e**) by Au(PEt₃)Cl using equilibrium dialysis. The metal content was determined by ICP-MS. **f** Relative ExoN activity of SARS-CoV-2 nsp14 in the presence of Zn-nsp10 and Au(I)-nsp10. **g–h** CD spectrum (**g**) and quan-

titative estimation of the secondary structure contents (**h**) of nsp14 in the presence of different molar equivalents of Au(PEt₃)Cl. **i** Size-exclusion chromatography profiles of native-nsp14 in the presence of increasing molar equivalents of Au(PEt₃)Cl. The elution volumes and corresponding molecular masses of the standards are shown based on the calibration using gel filtration. All data are presented as mean values \pm SD ($n=3$)

the proposed noncompetitive mode of inhibition of Au(I) on the ExoN activity of nsp14/nsp10.

In the MTase reaction of nsp14, we used S-adenosyl methionine (SAM) as the methyl donor and G(5')ppp(5') A RNA cap structure analog as the methyl recipient. The kinetic assays were also conducted in the presence of increasing concentrations of these two substrates, i.e., SAM and G(5')ppp(5')A RNA analog. Reaction progress was monitored by calculating the production of the reaction product S-adenosylhomocysteine (SAH). For the SAM-dependent kinetic assay, increasing molar equivalents of Au(I) revealed an unchanged K_m value of 1.62 ± 0.02 μ M, whereas an apparent decrease in V_{max} values from 0.16 to 0.09 μ M min⁻¹ (Fig. 5b). We also observed similar trends in the G(5')ppp(5')A RNA-dependent kinetic assay, where the K_m values remained unchanged at 1.18 ± 0.02 μ M; whereas V_{max} values decreased from 0.15 to 0.12 μ M min⁻¹ (Fig. 5c), indicative of a noncompetitive inhibition of Au(I) on MTase activity of nsp14.

Since nsp14 and nsp10 have 3 and 2 zinc-finger motifs respectively, playing structural roles and as well as being important to the functions of nsp14/nsp10 complex. The

soft nature of Au(I) makes it very likely to bind to the thiolates/nitrogen atoms in these cysteine/histidine-rich zinc-binding sites. To verify this, we then investigated the binding of Au(I) to the native nsp14 and nsp10 using equilibrium dialysis and determined the metal contents by inductively coupled plasma mass spectrometry (ICP-MS). As shown in Fig. 5d, e, the supplementation of increasing amounts of Au(I) (as Au(PEt₃)Cl) to the intact proteins resulted in *ca.* 2.95 ± 0.23 mol equiv of Au(I) bound to per nsp14 at the expense of *ca.* 2.56 ± 0.21 mol equiv of Zn(II) release. Similarly, *ca.* 1.84 ± 0.66 mol equiv of Au(I) bound to per nsp10, accompanied by *ca.* 1.89 ± 0.28 mol equiv of Zn(II) release. By fitting the data to the specific binding plot, the dissociation constants (K_d) were calculated to be 6.54 ± 0.33 μ M and 6.55 ± 0.77 μ M and the maximal binding capacity (B_{max}) were calculated to be 3.10 ± 0.32 and 1.75 ± 0.60 for nsp14 and nsp10 respectively, indicative of 3 and 2 Au(I) bound to nsp14 and nsp10 respectively, leading to 3 and 2 Zn(II) ions release, respectively. In addition, since the ExoN activity of nsp14 is largely stimulated by nsp10, and nsp10–nsp14 intermolecular interaction involves residues around the zinc finger of nsp10 [33, 34], we also examined the influence of Au(I)

binding to nsp10 on the ExoN activity of nsp14. In contrast to native Zn(II)-bound nsp10, Au(I)-bound nsp10 could not stimulate the ExoN activity of nsp14 (Fig. 5f), suggesting that binding of Au(I) to nsp10 might disrupt its interaction with nsp14, which further abrogates the ExoN activity of nsp14. These results suggest that Au(I)-based compounds inhibit the activity of nsp14/nsp10 through displacing the essential Zn(II) ions from the enzymes.

Metals have diversified ionic radii as well as coordination geometry and numbers, thus interaction with different metals may result in changes in protein structures and/or configurations. We then further investigated the influence of Au(I) binding on the secondary and quaternary structures of nsp14. Circular dichroism (CD) spectroscopy was used to examine the protein secondary structure changes. CD spectrum of the purified nsp14 shows two negative bands at 222 nm and 208 nm and a positive band at around 190 nm, indicating the predominant presence of α -helix structure (Fig. 5g) [35]. The spectra were then deconvoluted by *BeStSel* (Beta Structure Selection) to do the secondary structure determination and fold recognition [36], and the estimated α -helix structure content was around 65% in nsp14, as shown in Fig. 5h. Significantly, treatment of Au(I) resulted in less negative bands at 222 nm and 208 nm for the protein. Specifically, devolution of the CD spectrum revealed that after treatment with Au(I), the helix content in nsp14 was decreased to 36%, indicative of an obvious secondary structure change on nsp14 upon Au(I) binding. We also investigated the influence of Au(I) on the quaternary structure of nsp14 by size-exclusion chromatography. As shown in Fig. 5i, in the absence of Au(I), the intact nsp14 was eluted at 9.6 mL, corresponding to a molecular weight of 60 kDa (i.e. monomeric state). After incubating nsp14 with increasing molar equivalents (0–10) of Au(I), we observed the

decreased intensities at the elution volume of 9.6 mL (i.e. monomer peaks), and appearance and increase in the peaks at an elution volume of *ca.* 9.1 mL, suggesting that Au(I) led to partial oligomerization of nsp14. Taken together, we demonstrate that the inhibitory effect of Au(I)-based compounds on nsp14/nsp10 activity is attributable to the displacement of essential Zn(II) ion in nsp14/nsp10 by Au(I), which leads to the secondary and quaternary structure changes on the protein.

Au(I) compounds inhibit nsp13 activity via displacement of essential Zn(II), disrupting the binding of SARS-CoV-2 nsp13 to ATP

Nsp13 also consists of 3 zinc finger sites at its N-terminal zinc-binding domain. Therefore, we first investigated whether Au(I) could interact with zinc fingers in nsp13 by equilibrium dialysis. Our ICP-MS results show that after the addition of increasing amount of Au(I) (as Au(PET₃)Cl), the native nsp13 could release *ca.* 2.88 ± 0.18 mol equiv of Zn(II) and instead bind with *ca.* 2.97 ± 0.20 mol equiv of Au(I) (Fig. 6a). By nonlinear fitting to the specific binding plot, K_d was calculated to be 2.29 ± 0.22 μ M and B_{max} was calculated to be 3.33 ± 0.11 respectively, indicative of 3 Au(I) bound to nsp13, leading to 3 Zn(II) ions release, respectively.

To further explore the mechanism of Au(I)-based compounds against SARS-CoV-2 helicase activities, we then examined whether binding of Au(I) to nsp13 disrupt the binding of ATP to the enzyme by using adenosine 5'-O-(3-thiotriphosphate) (BODIPYTM FL ATP- γ -S), a hydrolysis resistant ATP analogue. When BODIPY ATP- γ -S binds to ATP-binding proteins, the quenched fluorescence will recover. We pre-incubated nsp13 with

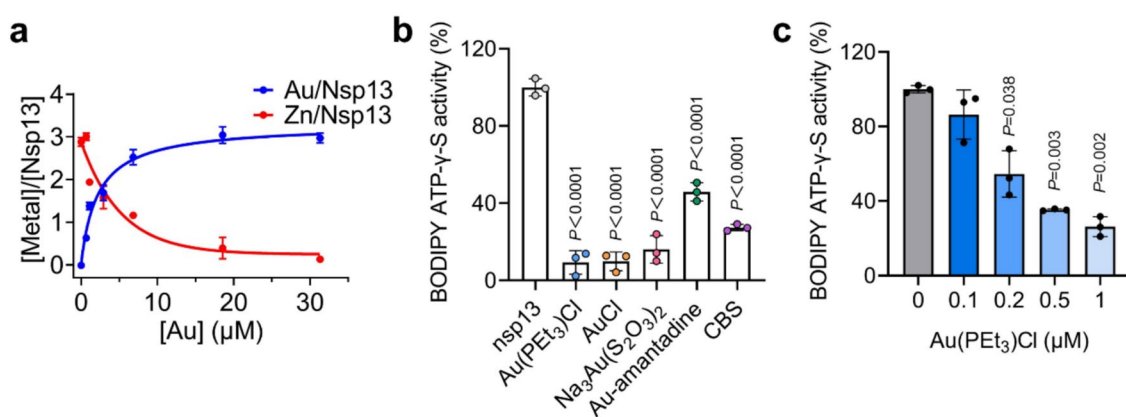


Fig. 6 Au(I) inhibits SARS-CoV-2 helicase activities by displacing its essential Zn(II) and disrupting its binding to ATP. **a** The substitution of Zn(II) in native nsp13 by Au(PET₃)Cl using equilibrium dialysis. The metal content was determined by ICP-MS. **b** Fluorescence intensity of BODIPYTM FL ATP- γ -S in the presence of nsp13 with

and without selected Au(I)-based compounds. **c** Dose-dependent inhibition of Au(PET₃)Cl in fluorescence intensity of BODIPYTM FL ATP- γ -S. All data are shown as mean \pm SD. Statistical significance was calculated by an unpaired two-tailed Student's *t*-test ($n=3$), * $P < 0.05$, ** $P < 0.01$ and *** $P < 0.001$

1 μM selected Au(I)-based compounds ($\text{Au}(\text{PET}_3)\text{Cl}$, AuCl , $\text{Na}_3\text{Au}(\text{S}_2\text{O}_3)_2$ and Au-amantadine) for 10 min at room temperature, then mixed with 10 nM BODIPYTM FL ATP- γ -S, where CBS was used as a positive control. As shown in Fig. 6b, the fluorescence intensity decreased in all Au(I) treated groups, confirming the Au(I)-based compounds were able to disrupt SARS-CoV-2 nsp13 binding to ATP. $\text{Au}(\text{PET}_3)\text{Cl}$ was also used as a showcase to evaluate the dose-dependent inhibitory effect of Au(I)-based compounds. The fluorescence intensity decreased in a dose-dependent manner upon treatment with 0.1, 0.2, 0.5 and 1 μM $\text{Au}(\text{PET}_3)\text{Cl}$ (Fig. 6c).

Subsequently, we determined whether Au(I)-based compounds also inhibit the binding between dsDNA and protein by EMSA [21, 37]. We preincubated 2 μM nsp13 with different concentrations (0, 2, 10 and 20 μM) of $\text{Au}(\text{PET}_3)\text{Cl}$ for 2 h at room temperature, then incubated with 100 nM DNA substrate to form the protein-dsDNA complex. EMSA gel image indicated Au(I) did not disrupt the binding of protein to dsDNA (Fig. S3). Collectively, we show that the Au(I)-based compound inhibits SARS-CoV-2 helicase activities by displacing the critical Zn(II) ions from its zinc-finger sites by Au(I) ions, which can disrupt the binding of protein to ATP instead of dsDNA, resulting in insufficient energy supporting unwinding activity.

Conclusions

We have demonstrated Au(I)-based compounds as effective anti-SARS-CoV-2 agents by targeting both nsp14/nsp10 complex and nsp13. The pan-anti-SARS-CoV-2 activity of Au(I) drugs was validated in infected mammalian cell. By evaluating the ExoN and MTase activities of nsp14 as well as ATPase and DNA unwinding activities of nsp13 (helicase), we found certain Au(I)-based compounds exhibited excellent effect on inhibition of both nsp14/nsp10 and nsp13, with IC_{50} as low as less than 1 μM . Mechanistic studies showed that Au(I) compounds could inhibit nsp14/nsp10 and nsp13 activity through displacing its essential Zn(II) from the proteins by Au(I). Such metal displacement features led to secondary and quaternary structural changes of nsp14 as well as disruption of the binding of nsp13 to ATP, subsequently resulting in insufficient energy support for DNA unwinding. Taken together, our study demonstrates the importance of nsp14/nsp10 and nsp13 as the targets for Au(I)-based anti-SARS-CoV-2 agents, thus the development of effective Au(I)-based inhibitors against nsp14/nsp10 and nsp13 will be an effective strategy for combating SARS-CoV-2 and its variants due to their multi-target properties. Nevertheless, further work is required to examine the activity in vivo as well as ADME and toxicity in animals.

Materials and methods

Chemicals

Colloidal bismuth subcitrate (CBS) were prepared as described previously [19]. BODIPYTM FL ATP- γ -S was from Invitrogen. Certain Au(I) drugs/compounds were purchased from Sigma-Aldrich and the other 14 Au(I)-based compounds were synthesized by ourselves. All chemicals were purchased from Thermo Fisher unless otherwise stated.

Synthesis of Au(I)-based compounds

General procedures for preparing substituted thiourea

Various amine (1.7 mmol) was dissolved in DCM, 1,1'-Thiocarbonyldiimidazole (TCDI) (1.9 mmol) was then added, the solution was stirred for 3 h, 20 eq. of 28% NH_3 solution was then added and stirred overnight. NH_3 was neutralized by 2 M HCl and 50 ml DCM was added, the organic layer was extracted with 2N HCl, the organic layer was then collected and rotary evaporated. Column chromatography (1:1 hexane: EA) was performed to give substituted thiourea.

General procedures for thiourea conjugate with Au(I)

Various thiourea (0.285 mmol) was dissolved in methanol, chloro(triethylphosphine)gold(I) (0.285 mmol) were added, the mixture was heated to 60 $^{\circ}\text{C}$ overnight. The solvent was then rotary evaporated and recrystallized in methanol/diethyl ether solution to yield thiourea conjugate with Au(I) complexes.

General procedures for thiol conjugated with Au(I)

To a solution of chloro(triethylphosphine)gold(I) (0.285 mmol) in methanol, various thiol (0.285 mmol) was added, followed by NaOMe (0.285 mmol, 1 equiv. for thiol), the solution was stirred overnight. The solvent was then rotary evaporated and redissolved in ethyl acetate, the organic layer was extracted with water or 1N HCl for carboxylate-containing ligand, the organic layer was then collected and rotary evaporated to give thiol conjugated with Au(I) complexes.

General procedures for dithiocarbamate conjugated with Au(I)

To a solution of chloro(triethylphosphine)gold(I) (0.285 mmol) in methanol, various dithiocarbamate sodium salt or potassium salt (0.285 mmol) was added, the solution

was heated to 60 °C overnight. The solvent was then rotary evaporated and redissolved in DCM, the organic layer was extracted with water, the organic layer was then collected and rotary evaporated to give dithiocarbamate conjugated with Au(I) complexes.

1-(adamantan-1-yl)thiourea (1)

Synthesized using General procedures for preparing substituted thiourea. (62.1% yield). ^1H NMR (400 MHz, CDCl_3): δ 5.91–6.22 (bs, 2H), δ 4.81 (s, 1H), δ 2.15 (t, 1H), δ 2.10 (d, 3H), δ 1.65–1.73 (m, 4H), δ 1.59 (s, 8H).

Au-amantadine (2)

(1-(adamantan-1-yl)thiourea)-(triethylphosphine)-gold(I) was synthesized using General procedures for thiourea conjugated with Au(I). (94.6% yield). ^1H NMR (400 MHz, $\text{DMSO}-d_6$): δ 1.93–2.07 (s + s + s, 10H), δ 1.87–1.92 (tt, 6H), δ 1.56–1.64 (dt, $J = 12$ Hz, 4 Hz, 6H), δ 1.04–1.12 (qq, 9H). ^{13}C NMR (400 MHz, $\text{DMSO}-d_6$): δ (ppm) 8.98, 16.73, 16.98, 28.9, 35.72, 40.04, 40.69, 52.85, 180.59. ESI-MS (+) m/z 525.1740, found for $\text{C}_{17}\text{H}_{33}\text{N}_2\text{PSAu} [\text{M}]^+$ (calcd: 525.1762).

Au-DEDC (3)

((diethylcarbamothioyl)thio)-(triethylphosphine)-gold(I) was synthesized using General procedures for dithiocarbamate conjugated with Au(I) with sodium diethyldithiocarbamate trihydrate. (62.3% yield). ^1H NMR (400 MHz, $\text{DMSO}-d_6$): δ 3.79–3.80 (q, 4H), δ 1.85–1.88 (quin, 6H), δ 1.18–1.20 (m, 6H), δ 1.09–1.15 (m, 9H). The NMR data align with previous publication [38].

Au-thiourea (4)

(2-amino-7H-purine-6-thioate)-(triethylphosphine)-gold(I) was synthesized using General procedures for thiol conjugated with Au(I). (64% yield). ^1H NMR (400 MHz, $\text{DMSO}-d_6$): δ 12.265 (bs, 1H), δ 7.752 (bs, 1H), δ 5.934 (bs, 1H), δ 1.87–1.95 (q, 6H), δ 1.13–1.21 (tt, 9H). ^{13}C NMR (400 MHz, $\text{DMSO}-d_6$): δ (ppm) 8.77, 17.25, 17.47, 126.19, 137.18, 151.07, 159.22, 170.94. ESI-MS (+) m/z 482.0841, found for $\text{C}_{11}\text{H}_{19}\text{N}_5\text{PSAu} [\text{M} + \text{H}]^+$ (calcd: 482.0843).

Au-Pme-thiourea (5)

((amino(iminio)methyl)thio)-(trimethylphosphine)-gold(I) was synthesized using General procedures for thiourea conjugate with Au(I). (94% yield). ^1H NMR (400 MHz, D_2O): δ 1.61 (s, 1H), δ 1.64 (s, 1H). ^{13}C NMR (400 MHz, D_2O): δ (ppm) 13.85, 14.10, 15.05, 15.51, 175.32. ESI-MS (+)

m/z 349.0188, found for $\text{C}_4\text{H}_{13}\text{N}_2\text{PSAu}^+ [\text{M}]^+$ (calcd: 349.0197).

Au-6TG (6)

((amino(iminio)methyl)thio)-(triethylphosphine)-gold(I) was synthesized using General procedures for thiourea conjugate with Au(I). (91.4% yield). ^1H NMR (400 MHz, D_2O): δ 1.04–1.12 (tt, 9H), δ 1.83–1.91 (qq, 6H). ^{13}C NMR (400 MHz, D_2O): δ (ppm) 8.3, 16.8, 17.04, 176.34. ESI-MS (+) m/z 391.0661, found for $\text{C}_7\text{H}_{19}\text{N}_2\text{PSAu}^+ [\text{M}]^+$ (calcd: 391.0667).

2-isonicotinoylhydrazine-1-carbodithioate (7)

Isoniazid (1 g, 7.3 mmol) was dissolved in methanol was then added NaOH (0.3 g, 7.4 mmol), CS_2 (0.427 ml, 7.4 mmol) was added dropwise, the mixture was then stirred overnight. The solvent was then rotary evaporated and redissolved in a minimum amount of methanol and then added diethyl ether, and the pale-yellow ppt. was collected. ^1H NMR (400 MHz, $\text{DMSO}-d_6$): δ 8.58–8.68 (dd, 2H), δ 7.69–7.71 (dd, 2H).

Au-isoniazid (8)

(2-isonicotinoylhydrazine-1-carbodithioate)-(triethylphosphine)-gold(I) was synthesized using General procedures for dithiocarbamate conjugated with Au(I). (50% yield). ^1H NMR (400 MHz, CDCl_3): δ 8.76 (d, 2H), δ 7.85 (d, 2H), δ 1.89–1.97 (qq, 6H), δ 1.20–1.29 (tt, 9H). ^{13}C NMR (400 MHz, CDCl_3): δ (ppm) 9.67, 17.75, 18.05, 119.31, 121.47, 140.7, 150.67, 151.09. TGA analysis: 64.5% weight loss at 750 °C in compress air, proposed structure: $[\text{Au}(\text{PEt}_3)(\text{isoniazid}-\text{CS}_2)]$.

(S)-1-((3-(3-fluoro-4-morpholinophenyl)-2-oxooxazolidin-5-yl)methyl)thiourea (9)

Synthesized using General procedures for preparing substituted thiourea (57.1%). ^1H NMR (400 MHz, $\text{DMSO}-d_6$): δ 7.918 (t, 1H), δ 7.48–7.52 (d, 1H), δ 7.17–7.20 (bs + d, 2H), δ 7.04–7.06 (t, 1H), δ 4.83 (t, 1H), δ 4.07–4.12 (t, 1H), δ 3.80 (s, 4H), δ 3.73 (t, 4H), δ 2.96 (t, 4H).

Au-linezolid (10)

(S)-((((3-(3-fluoro-4-morpholinophenyl)-2-oxooxazolidin-5-yl)methyl)amino)(iminio)methyl)thio)-(triethylphosphine)-gold(I) was synthesized using General procedures for thiourea conjugate with Au(I) (94.5% yield). ^1H NMR (400 MHz, $\text{DMSO}-d_6$): δ 7.93 (t, 1H), δ 7.48–7.52 (d, 1H), δ 7.17–7.20 (bs + d, 2H), δ 7.04–7.06 (t, 1H), δ 4.83 (t, 1H), δ 4.07–4.12 (t, 1H), δ 3.80 (s, 2H), δ

3.73 (t, 4H), δ 3.31 (s, 2H), δ 2.96 (t, 4H), δ 1.88–1.97 (tt, 6H), δ 1.05–1.14 (qq, 9H). ^{13}C NMR (400 MHz, DMSO- d_6): δ (ppm) 8.98, 16.74, 16.99, 45.53, 46.94, 50.69, 66.14, 71.62, 106.8, 106.78, 114.16, 119.25, 119.27, 133.33, 133.4, 135.55, 135.61, 153.75, 153.99, 155.36, 183.9. ESI-MS (+) m/z 669.1724, found for $\text{C}_{21}\text{H}_{34}\text{N}_4\text{O}_3\text{FPSAu}^+$ $[\text{M}]^+$ (calcd: 669.1733).

Au-NAC (11)

(N-acetyl cysteineate)-(triethylphosphine)-gold(I) was synthesized using General procedures for thiol conjugate with Au(I) (75% yield). ^1H NMR (400 MHz, DMSO- d_6): δ 7.88 (bs, 1H), δ 4.22–4.23 (d, $J=4$ δ 81.87–1.91 (tt + s, 9H), δ 1.05–1.15 (qq, 9H). The NMR align with the previous publication [39, 40].

Thiophene-Au-Cl (12)

Tetrachloroauric(III) acid trihydrate (1.0 g, 2.5 mmol) was dissolved in 2 ml of water and diluted with 10 ml of ethanol. To the resultant solution, tetrahydrothiophene (0.44 mL, 5 mmol) was added dropwise, after addition the mixture was stirred at room temperature for 2 h, and then a white precipitate appeared. The precipitate was collected by filtration, washed with small amounts of ethanol and then diethyl ether to give 0.72 g (2.2 mmol) of white solid (94% yield). ^1H NMR (400 MHz, CDCl_3): δ 3.45 (d, 2H), δ 2.28 (d, 2H). ^{13}C NMR (200 MHz, CDCl_3): δ 40.4, 30.5. The NMR data aligns with previous publications [41].

Urotropine-Au-Cl (13)

Thiophene-Au-Cl (0.1 g, 0.31 mmol) was dissolved in 5 ml methanol and 1,3,5-triaza-7-phosphaadamantane (0.05 g, 0.31 mmol) was added in ice-bath. The solvent and thiophene were removed by blowing compressed air into the mixture after 3 h of reaction time. The residue was recrystallized in water/acetone mixture to give a pale-yellow cpd. (77% yield). ^1H NMR (400 MHz, DMSO- D_6): δ 4.33 (s, 7H), 4.36 (s, 2H), δ 4.49 (s, 2H), δ 4.51 (s, 1H). ^{13}C NMR (400 MHz, DMSO- D_6): δ 40.04, 50.82, 50.98, 71.77, 71.82. The NMR data aligns with previous publication [42].

Au-GSH (14)

((R)-2-((S)-4-amino-4-carboxybutanamido)-3-((carboxymethyl)amino)-3-oxopropyl)thiolate)-(triethylphosphine)-gold(I) was synthesized using General procedures for thiol conjugated with Au(I) (47.6% yield). Recrystallized in MeOH: diethyl ether as a white precipitate. ^1H NMR (400 MHz, DMSO- D_6): δ 8.17 (s, 1H), δ 4.21–4.23 (d, $J=8$ Hz, 2H), δ 3.60–3.61 (d, $J=4$ Hz, 2H), δ 3.33–3.37

(t, $J=8$ Hz, 1H), δ 3.06 (m, 2H), δ 2.89 (m, 1H), δ 2.24–2.39 (m, 2H), δ 1.82–1.90 (m + tt, 7H), δ 1.04–1.12 (qq, 9H). The NMR data align with previous publication [40].

Au- N_2S (15)

((1H-imidazol-2-yl)thiolate)gold-(triethylphosphine)-gold(I) was synthesized using General procedures for thiol conjugate with Au(I) (57.5% yield). ^1H NMR (400 MHz, CDCl_3): δ 6.89 (s, 2H), δ 1.85–1.93 (tt, 6H), δ 1.16–1.25 (qq, 9H). ^{13}C NMR (400 MHz, CDCl_3): δ (ppm) 9.03, 17.54, 17.77, 121.4, 146.4, 177.24. ESI-MS (+) m/z 415.0665, found for $[\text{C}_9\text{H}_{18}\text{N}_2\text{PSAu} + \text{H}]^+$, $[\text{M} + \text{H}]^+$ (calcd: 415.0666).

Carbazole-thiourea (16)

1-(9-ethyl-9H-carbazol-3-yl)thiourea was synthesized using General procedures for preparing substituted thiourea (75.4%). ^1H NMR (400 MHz, DMSO- d_6): δ 9.63 (s, 1H), δ 8.13–8.15 (d, $J=8$ Hz, 1H), δ 8.03 (s, 1H), δ 7.47–7.61 (t, $J=8$ Hz, 2H), δ 7.44–7.46 (t, $J=4$ Hz, 1H), δ 7.30–7.32 (d, $J=8$ Hz, 1H), δ 7.17–7.20 (t, $J=8$ Hz, 2H), δ 4.41–4.46 (q, $J=8$ Hz, 2H), δ 1.29–1.31 (t, $J=8$ Hz, 3H).

Au-carb (17)

1-(9-ethyl-9H-carbazol-3-yl)isothiuronium)-(triethylphosphine)-gold(I) was synthesized using General procedures for thiourea conjugate with Au(I) (89.5% yield). ^1H NMR (400 MHz, DMSO- d_6): δ 8.14–8.17 (d, $J=8$ Hz, 1H), δ 8.04–8.06 (t, $J=8$ Hz, 1H), δ 7.56–7.62 (q, $J=4$ Hz, 2H), δ 7.44–7.46 (t, $J=4$ Hz, 1H), δ 7.31–7.33 (d, $J=8$ Hz, 1H), δ 7.19–7.22 (t, $J=4$ Hz, 2H), δ 4.41–4.46 (q, $J=8$ Hz, 2H), δ 1.85–1.93 (tt, 6H), δ 1.29–1.31 (t, $J=8$ Hz, 3H), δ 1.03–1.08 (qq, 9H). ^{13}C NMR (400 MHz, DMSO- d_6): δ (ppm) 8.92, 13.73, 16.88, 16.92, 37.01, 109.2, 109.28, 117.2, 118.75, 126.0, 121.97, 122.22, 123.72, 125.97, 129.73, 137.65, 139.96, 179.57. ESI-MS (+) m/z 584.1559, found for $[\text{C}_{21}\text{H}_{30}\text{N}_3\text{PSAu}]^+$, $[\text{M}]^+$ (calcd: 584.1558).

Au-Se (18)

((amino(iminio)methyl)seleno)-(triethylphosphine)-gold(I) was synthesized using General procedures for preparing substituted thiourea (75.4%). ^1H NMR (400 MHz, D_2O): δ 1.83–1.91 (tt, 6H), δ 1.04–1.13 (qq, 9H). ESI-MS (+) m/z 439.0118, found for $[\text{C}_7\text{H}_{19}\text{N}_2\text{PSeAu}]^+$, $[\text{M}]^+$ (calcd: 439.0111).

Cell lines and viruses

VeroE6-TMPRSS2 cells were cultured in Dulbecco's Modified Eagle Medium (DMEM), 10% fetal bovine serum (FBS)

and 1% antibiotics (penicillin and streptomycin) at 37 °C. All experiments involving live SARS-CoV-2 followed the approved standard operating procedures of the Biosafety Level 3 facility at the Department of Microbiology, The University of Hong Kong.

Cellular antiviral activity assay

A viral load reduction assay was performed for the evaluation of cellular antiviral activity, as described previously but with modifications [43, 44]. Briefly, SARS-CoV-2-infected (MOI=0.01) VeroE6-TMPRSS2 cell were treated with different concentrations of Au(I)-based compounds. The culture supernatants of the infected cell were harvested at 48 h-post-infection (h.p.i.) for analysis of viral replication. The supernatant was collected by 50 µL RLT buffer, and subsequently extracted for total RNA with the QIAamp viral RNA mini kit (Qiagen). Quantitative reverse transcription-polymerase chain reaction (qRT-PCR) was used for quantitation of SARS-CoV-2 viral load using the One Step TB Green® PrimeScript™ RT-PCR Kit II (Takara) with a LightCycler 480 Real-Time PCR System (Roche). The primers and probe sequences were against the RNA-dependent RNA polymerase/Helicase (RdRP/Hel) gene region of SARS-CoV-2: forward primer: 5'CGCATACAGTCTTRCAGGCT-3'; reverse primer: 5'-GTGTGATGTTGAWATGACATGGTC-3'; specific probe: 5'-FAMTTAAGA TGTGGTGCTTGCATACGTAGAC-IABkFQ-3'.

Plaque reduction assay

VeroE6-TMPRSS2 cells (2×10^5 per well) were seeded in 24-well plate. Next day, cells were infected with 50 plaque-forming units (PFU) of SARS-CoV-2 Omicron BA.5, then treated with the compounds in a dose-dependent manner or without drugs as control. Monolayers were then overlaid with media containing 1% low melting agarose inverted and incubated for another 72 h. Then, the wells were fixed with 10% formaldehyde for 12 h. After removal of the agarose plugs, monolayers were stained with 0.7% crystal violet and plaques were counted.

Cloning, protein expression, and purification

SARS-CoV-2 nsp10 and nsp14 were overexpressed and purified as previously described [19]. Firstly, plasmids pET28a-nsp10 and pET28a-nsp14 were generated by cloned full-length nsp10 and nsp14 of SARS-CoV-2 isolate Wuhan-Hu-1, complete genome (NCBI GenBank accession no. NC_045512.2) into pET-28-a(+) vector with a N-terminal 6×His-tag, respectively. Next, the plasmids were transformed into *E. coli* DH10B and validated by sequencing. After validation, plasmids were then transformed

into Rosetta (DE3) pLysS, respectively. Cells containing pET28a-nsp10 and pET28a-nsp14 were cultured at 37 °C overnight in 2×YT medium supplemented with 50 µg·ml⁻¹ kanamycin and 20 µg·ml⁻¹ chloramphenicol, respectively. Then, cells were amplified at 37 °C in 2×YT medium at a 100-fold dilution and when OD₆₀₀ reached 0.7, the nsp10 and nsp14 were overexpressed by induction of 0.05 mM and 0.3 mM isopropyl β-D-thiogalactoside (IPTG) for nsp10 and nsp14, respectively. After induction for 18 h 16 °C with agitation at 160 rpm, cells were harvested by centrifugation at 5000g for 30 min at 4 °C, washed twice with phosphate-buffered saline (PBS), and then resuspended and lysed by sonication in bacteria lysis buffer (PBS containing 5 mM β-mercaptoethanol (only for nsp10), 0.1% Triton X-100, 1 mM phenylmethylsulfonyl fluoride (PMSF), 40 mM imidazole, and 10 mg/ml DNase I). The cell lysates were then centrifuged at 15,000 g for 45 min at 4 °C, and recombinant nsp10 and nsp14 were purified using Ni-NTA column (Invitrogen) using a gradient of imidazole-containing Tris-NaCl buffer (50 mM Tris-HCl, pH 7.5, 300 mM NaCl, 5 mM MgSO₄) for washing and elution. Thrombin Protease was used to remove His tags from nsp10 and nsp14. Further, nsp10 was purified by a Superdex 200 Increase 10/300 GL column (GE Life Sciences) with gel-filtration buffer (20 mM HEPES, pH 7.4, 150 mM NaCl, 5 mM MgCl₂, 5% glycerol), and nsp14 was purified using HiTrap S ion-exchange chromatography (GE Healthcare). Purified nsp10 and nsp14 were examined by SDS-PAGE and the identity of the proteins was further confirmed by LC-MS after trypsin digestion. Finally, proteins were aliquoted and stored in HEPES buffer (20 mM HEPES, pH 7.4, 150 mM NaCl, 5 mM MgCl₂ and 5% glycerol) at -80 °C for further use.

SARS-CoV-2 helicase was overexpressed and purified as previously described [20, 21]. Briefly, *E. coli* BL-21(DE3) cells harboring pET-28a-nsp13 plasmid were cultured in LB medium with 50 µg/mL kanamycin overnight and then diluted by 1:100 to 4 L fresh LB medium. Cells were cultured to OD₆₀₀ of 0.6–0.8, then induced by 200 µM IPTG at 16 °C for 18 h with agitation at 200 rpm. The bacteria were collected at 6000 g, 4 °C for 30 min. Cell pellets were resuspended in lysis buffer (20 mM Tris, 500 mM NaCl, pH 7.4, 0.1% Triton X-100) with Protease Inhibitor Cocktail and sonicated. The cell lysate was centrifuged (12,000g, 4 °C for 10 min), proteins was purified by Ni-NTA Agarose (Invitrogen). SARS-CoV-2 helicase was eluted by 250 mM imidazole and checked by SDS-PAGE. The purest fractions were removed His₆-tag by thrombin. The protein concentrations were quantified by a bicinchoninic acid (BCA) assay kit.

Methyltransferase (MTase) activity assay

A MTase-Glo™ Methyltransferase Assay Kit (Promega) was used to measure the MTase activity and a G(5')ppp(5')

A RNA Cap Structure Analog (New England Biolabs) was used as the substrate for the assay. Progression of the reactions was monitored by luminescence in white 384-well plates (Corning) using a SpectraMax iD3 multimode microplate reader.

For primary screening, before the methyltransferase reaction, nsp14 (5 μM) was pre-incubated with Au(I) drugs (250 μM) at room temperature for 1 h. Next, 8 μL reactions were carried out by incubating 1 μM nsp14 treated with a serial dilution of drugs, 20 μM for SAM and 20 μM for G(5')ppp(5')A RNA Cap Structure Analog in MTase reaction buffer (20 mM Tris-HCl, pH 8.0, 50 mM NaCl, 3 mM MgCl_2 , 0.1 mg/mL BSA, 0.5 mM TCEP) at room temperature for 30 min. Then, a 2 μL 5 \times Methyltransferase-Glo Reagent was added and the reactions were incubated at room temperature for 30 min. After that, 10 μL of Methyltransferase-Glo Detection Solution were added, followed by incubation for another 30 min at room temperature. The progress of the reactions was then monitored by luminescence using a microplate reader.

For determination of the half-maximum inhibitory concentration (IC_{50}), firstly, nsp14 (10 μM) was pre-incubated with Au(I) drugs (0, 0.5, 5, 10, 20, 50, 100, 200, 500, 1000 μM) at room temperature for 1 h before the methyltransferase reaction. Next, MTase reactions were carried out and detected as described in primary screening. Luminescence was then monitored by a microplate reader and dose-dependent inhibition curves were generated and IC_{50} value were calculated by nonlinear regression using GraphPad Prism.

For the MTase kinetic assays, an SAH standard curve was first generated to assess the linearity of the assay and to calculate the amount of the reaction product SAH produced in each reaction. 8 μL of MTase reaction buffer containing serial diluted SAH (from 0 to 1 μM) were incubated with 2 μL of 5 \times Methyltransferase-Glo Reagent for 30 min at room temperature followed by the addition of 10 μL of detection solution as described above. Luminescence was recorded and then plotted against SAH concentration by linear regression using GraphPad Prism. For methyltransferase kinetic reaction, nsp14 (5 μM) was pre-incubated with Au(I) drugs (as $\text{Au}(\text{PET}_3)\text{Cl}$) at the molar ratio (as indicated in the data) at room temperature for 1 h. MTase kinetic assays were carried out in 8 μL of MTase reaction buffer containing drug-treated nsp14 (1 μM), 2 μL 5 \times Methyltransferase-Glo Reagent, together with 25 μM G(5')ppp(5')A RNA Cap Structure Analog and serially diluted SAM (0, 0.5, 1, 2, 5, 10, 20 and 50 μM) for SAM-dependent kinetic assays, or 25 μM SAM and serially diluted G(5')ppp(5')A RNA Cap Structure Analog (0, 0.5, 1, 2, 5, 10, 20 and 50 μM) for G(5')ppp(5')A RNA-dependent kinetic assays at room temperature for 10 min, followed by adding 2 μL 0.5% trifluoroacetic acid (TFA) to stop the reaction. After that, 10

μL of Methyltransferase-Glo Detection Solution were added and mixed well, followed by incubation for another 30 min at room temperature. The control group was performed in the absence of drugs under the same condition. The amounts of SAH produced in different intervals were calculated by the standard curve to determine the velocity of the reaction. The velocity and the concentration of the substrates were used to generate the Lineweaver–Burk plot. K_m and V_{\max} were calculated by the Michaelis–Menten equation using GraphPad Prism.

FRET-based exoribonuclease (ExoN) activity assay

A slightly modified double-stranded RNA with a 20-nucleotide 5' dU overhang, conjugated to a Cy3-quencher (BHQ2) pair, was used as the substrate for the exoribonuclease activity assay based on a previous report (see Table S1) [45]. Nsp14 and nsp10 were mixed at a molar ratio of 1:4 to form the nsp14-nsp10 complex. Progression of the reactions was monitored by fluorescence ($\lambda_{\text{ex}} = 545 \text{ nm}$, $\lambda_{\text{em}} = 585 \text{ nm}$) in black 96-well plates (Thermo Fisher Scientific) using a SpectraMax iD3 multimode microplate reader. ExoN activities were calculated by the amount of fluorescence released after subtracting the initial reading.

For screening the inhibitor, 5 μM of nsp14-nsp10 complex were pre-incubated with 250 μM drugs at room temperature for 1 h. Then, the reaction was carried out in 20 μL of ExoN reaction buffer (50 mM Tris-HCl, pH 8.0, 30 mM NaCl, 2.5 mM MgCl_2 , 10 mM K_2HPO_4 , 0.5 mM tris(2-carboxyethylphosphine) (TCEP) and 0.1 mg/mL BSA) containing 200 nM nsp14/nsp10 complex, 10 μM drugs, and 50 nM Cy3/quencher-dsRNA substrates at 25 $^\circ\text{C}$ for 2 h. The fluorescence signal was monitored by the SpectraMax iD3 multimode microplate reader in real time.

For the half-maximum inhibitory concentration (IC_{50}) calculation, nsp14-nsp10 complex (10 μM) was pre-incubated with Au(I) drugs (0, 0.25, 1.25, 2.5, 5, 12.5, 25, 50, 125, 250, 500 and 1250 μM) at room temperature for 1 h before the nuclease reaction. Nuclease assays (20 μL) were performed at 25 $^\circ\text{C}$ for 2 h in ExoN reaction buffer in the presence of 50 nM Cy3/quencher-dsRNA substrates and 200 nM drug-pretreated nsp14/nsp10 complex. Dose–response curves for IC_{50} value were determined by nonlinear regression using GraphPad Prism.

For the ExoN kinetic assays, nsp14-nsp10 complex (10 μM) was incubated with an equal volume of drugs at the specified molar ratio for 2 h on ice before the nuclease reaction. Nuclease kinetic assays were carried out in 100 μL ExoN reaction buffer containing 100 nM (for RBC) and 50 nM (for $\text{Au}(\text{PET}_3)\text{Cl}$) nsp14-nsp10 complex incubated with drugs, and serially diluted Cy3/quencher-dsRNA substrates (0, 25, 50, 75, 100, 150, 200, 300, 400 and 500 nM). The control group was performed in the absence of drugs

under the same condition. The maximum of the first derivative over the first hour was calculated to determine the velocity of the reaction. The velocity was plotted against the concentration of the substrates. Slopes were then used to calculate the K_m and V_{max} by nonlinear fitting to the Michaelis–Menten equation using GraphPad Prism.

ATPase assay

ATPase inhibitory activities of gold-based compounds against SARS-CoV-2 helicase were assayed using a commercial assay kit (ab234055, Abcam). The experiments were performed following the manufacturer's instruction. In brief, we pre-incubated 20 nM nsp13 with different drugs/ concentrations drugs in a 50 μ L ATPase reaction buffer for 10 min at room temperature. Next, the other 50 μ L ATPase reaction buffer which included 1 μ L substrate was added into the reaction system for 20 min. Finally, 15 μ L developer was added to the well to react with the released phosphate. After 30 min incubation, the absorbance was measured by SpectraMax iD3 Multi-Mode microplate reader at 650 nm. The IC_{50} values were determined by nonlinear regression using GraphPad Prism. The assays were performed in triplicate.

FRET DNA duplex unwinding assay

The FRET-based DNA unwinding activity assay was performed as the previously described method [21, 46]. DNA oligos were purchased from Integrated DNA Technologies (see Table S1). The two oligomers mixed at a ratio of FL-Cy3: RL-BHQ of 1:1.5 for the final concentrations of 10 μ M and 15 μ M, respectively were annealed in annealing buffer containing 20 mM Tris–HCl pH 8.0, 150 mM NaCl by heating to 90 °C for 2 min in thermocycler (S1000™ Thermal Cycler, Bio-Rad), then cooling slowly to 25 °C at the rate of ~1 °C/min. 20 nM protein was pre-incubated with different metallodrug / concentrations in 95 μ L reaction buffer (20 mM Tris–HCl buffer, pH 7.4, 150 mM NaCl, 5 mM $MgCl_2$, 5 mM TCEP, 0.1 mg/ml BSA and 10% glycerol) in a 96-well black polystyrene microplate for 10 min at 25 °C. Then, 2 μ L 100 mM ATP, oligomers (FL-Cy3, RL-BHQ mixture) were added to result in the final concentration of FL-Cy3: RL-BHQ oligo and RL oligo at 5 nM and 50 nM respectively. Fluorescence intensity was measured at excitation/emission wavelengths 550/620 nm by SpectraMax iD3 Multi-Mode microplate reader. IC_{50} values were determined by nonlinear regression using GraphPad Prism. The assays were performed in triplicate.

Electrophoretic mobility shift assay (EMSA)

RNA-binding capability of nsp14 was determined by EMSA. For the protein dose-dependent RNA-binding assays of

nsp14, 200 nM of the ExoN substrate dsRNA were incubated with varying concentration of SARS-CoV-2 nsp14 (0, 0.4, 0.8, 1.2, 1.6, 2.0, 4.0, 8.0 μ M) in HEPES buffer at room temperature for 15 min. For the bismuth(III) and Au(I) addition assays, nsp14 (4 μ M) was pre-incubated with various concentrations of drugs (0, 1, 2, 4, 8, 20, 40 μ M) in HEPES buffer for 2 h on ice before the RNA-binding assays before incubating with 200 nM of dsRNA at room temperature for 15 min. A 20 μ L of the reaction mixture was then loaded onto 6% native-polyacrylamide gels and electrophoresed in 1xTBE buffer. Electrophoresis was carried out at 100 V for 50 min. Gels were subsequently stained by GelRed (Sigma Aldrich) for 5 min at room temperature and visualized through iBright™ CL750 Imaging System (Thermo Fisher Scientific).

EMSA for investigating the binding between nsp13 and DNA substrates was performed as previously reported [19]. Briefly, 2 μ M nsp13 was incubated with $Au(PEt_3)Cl$ in a dose-dependent manner in 20 μ L binding buffer (20 mM Tris pH 7.4, 20 mM NaCl, 1 mM TCEP, 5 mM $MgCl_2$) for 2 h at 25 °C. Then, incubated per sample at 37 °C with 100 nM dsDNA. After 15 min incubation, the reaction was stopped by 4 μ L loading buffer (50% glycerol, 0.02% bromophenol blue). The reaction mixture was electrophoresed in 8% native-polyacrylamide gels at 150 V for 1 h. The gel was stained by GelRed (Sigma Aldrich) for 10 min and images were captured by iBright™ CL750 Imaging System (Thermo Fisher Scientific).

Metal displacement analysis

Au(I) binding and Zn(II) release on nsp10 and nsp14 were determined by Inductively Coupled Plasma Mass Spectrometry (ICP-MS) on Agilent 7700x ICP-MS (Agilent Technologies). SARS-CoV-2 nsp14, nsp13 and nsp10 were incubated with 3 molar equivalents of $ZnSO_4$ in dialysis buffer (20 mM HEPES, pH 7.4, 150 mM NaCl, 5 mM $MgCl_2$, 5% glycerol, 0.5 mM TCEP) with mild shaking at 4 °C overnight, followed by removal of unbound zinc(II) in Zn-free dialysis buffer to make the fully Zn-bound proteins. Dialysis tubes loaded with 100 μ L Zn-bound proteins (5 μ M for nsp14 and nsp13 and 20 μ M for nsp10) or protein buffer were placed into 50 mL dialysis buffer in the presence of different concentrations of Au(I) compounds (as $Au(PEt_3)Cl$) with mild shaking at 18 °C overnight. The protein concentration was measured by bicinchoninic acid (BCA) assay, and the metal concentration of solution both inside and outside the dialysis tubes was determined by ICP-MS.

Circular dichroism (CD) spectroscopy

CD spectra were collected by a Jasco J-815 Spectrometer. Nsp14 (3 μ M) was incubated with indicated molar

equivalents of drugs (as $\text{Au}(\text{PEt}_3)\text{Cl}$) for 1 h on ice in 10 mM Na_2HPO_4 buffer (pH 7.0), respectively. CD Spectra were detected between 190 to 250 nm at room temperature in a 0.1 cm quartz cuvette with a scanning rate of 50 nm/min. Each spectrum was scanned for three times and then subjected to the online CD spectrum analysis server *BeStSel* [36].

Size-exclusion chromatography analysis

Size-exclusion chromatography was performed with a Superdex 75 increase 100/200 GL analytical column (Cytiva) at 4 °C. The column was pre-equilibrated by PBS buffer. 20 μM nsp10 or 5 μM nsp14 were pre-incubated with different molar equivalents of $\text{Au}(\text{PEt}_3)\text{Cl}$ for 1 h at 4 °C. Samples were prepared in PBS buffer to a final volume of 500 μL before loading to the column at a flow rate of 0.8 mL/min.

ATP- γ -S fluorescence assay

Pre-incubated 100 nM nsp13 with different drugs / concentrations of drugs in 50 μL reaction buffer (20 mM Tris, 500 mM NaCl, pH 7.4, 5 mM MgCl_2) for 10 min at room temperature. Then, 10 nM BODIPYTM FL ATP- γ -S was added. Fluorescence signals were measured by SpectraMax iD3 Multi-Mode microplate reader at excitation/emission wavelengths 502/545 nm. The assays were performed in triplicate. Data are shown as mean \pm SD. The statistical significance was calculated by unpaired two-tailed Student's *t*-test ($n=3$), * $P < 0.05$, ** $P < 0.01$, and *** $P < 0.001$.

Statistical analysis

All statistical analyses were performed on three independent experiments, or more if otherwise stated, using Prism 8.0 (GraphPad Software Inc.).

Supplementary Information The online version contains supplementary material available at <https://doi.org/10.1007/s00775-025-02118-9>.

Author contributions All authors contributed to the study conception and design. Material preparation, data collection and analysis were performed by J.C., X.W., C.L.C. and K.T. The first draft of the manuscript was written by J.C., X.W., and H.L., and all authors commented on previous versions of the manuscript. All authors read and approved the final manuscript.

Funding This work was partially supported by the Research Grants Council of Hong Kong (17306323, SRFS2122-7S04, 17318322, N_HKU767/22, C7002-23Y, T11-709/21N, G-HKU706/23), Hong Kong SAR; and the University of Hong Kong (URC and Norman & Cecilia Yip Foundation).

Data availability No datasets were generated or analysed during the current study.

Declarations

Conflict of interest The authors declare no competing interests.

Ethical Approval, Consent to Participate, and Consent to Publish declarations.

Not applicable.

Open Access This article is licensed under a Creative Commons Attribution 4.0 International License, which permits use, sharing, adaptation, distribution and reproduction in any medium or format, as long as you give appropriate credit to the original author(s) and the source, provide a link to the Creative Commons licence, and indicate if changes were made. The images or other third party material in this article are included in the article's Creative Commons licence, unless indicated otherwise in a credit line to the material. If material is not included in the article's Creative Commons licence and your intended use is not permitted by statutory regulation or exceeds the permitted use, you will need to obtain permission directly from the copyright holder. To view a copy of this licence, visit <http://creativecommons.org/licenses/by/4.0/>.

References

1. Yang H, Rao Z (2021) Structural biology of SARS-CoV-2 and implications for therapeutic development. *Nat Rev Microbiol* 19:685–700
2. Tan H, Hu Y, Jadhav P, Tan B, Wang J (2022) Progress and challenges in targeting the SARS-CoV-2 papain-like protease. *J Med Chem* 65:7561–7580
3. Cao B, Wang Y, Wen D, Liu W, Wang J, Fan G et al (2020) A trial of lopinavir-ritonavir in adults hospitalized with severe Covid-19. *N Engl J Med* 382:1787–1799
4. Recovery Collaborative Group (2020) Lopinavir-ritonavir in patients admitted to hospital with COVID-19 (RECOVERY): a randomised, controlled, open-label, platform trial. *Lancet* 396:1345–1352
5. Li G, De Clercq E (2020) Therapeutic options for the 2019 novel coronavirus (2019-nCoV). *Nat Rev Drug Discov* 19:149–150
6. Abdelnabi R, Foo CS, Jochmans D, Vangeel L, De Jonghe S, Augustijns P et al (2022) The oral protease inhibitor (PF-07321332) protects Syrian hamsters against infection with SARS-CoV-2 variants of concern. *Nat Commun* 13:719
7. Unoh Y, Uehara S, Nakahara K, Nobori H, Yamatsu Y, Yamamoto S et al (2022) Discovery of S-217622, a noncovalent oral SARS-CoV-2 3CL protease inhibitor clinical candidate for treating COVID-19. *J Med Chem* 65:6499–6512
8. Chaves OA, Sacramento CQ, Ferreira AC, Mattos M, Fintelman-Rodrigues N, Temerozo JR et al (2021) Atazanavir is a competitive inhibitor of SARS-CoV-2 M(pro), impairing variants replication in vitro and in vivo. *Pharmaceuticals* 15:21
9. Antiviral for adult patients hospitalized for SARS-CoV-2 infection: a randomized, Phase 2/3, multicenter, placebo controlled, adaptive, multi-arm, multi-stage clinical trial. (2020) National Library of Medicine (US). <https://clinicaltrials.gov/study/NCT04468087>. Accessed June 10, 2024
10. Notice Regarding the Progress of S-217622 to Fight COVID-19. (2022) SHIONOGI. <https://www.shionogi.com/global/en/news/2022/01/e-220120.html>. Accessed June 10, 2024
11. Sacco MD, Hu Y, Gongora MV, Meilleur F, Kemp MT, Zhang X et al (2022) The P132H mutation in the main protease of Omicron SARS-CoV-2 decreases thermal stability without compromising catalysis or small-molecule drug inhibition. *Cell Res* 32:498–500

12. Fact sheet for healthcare providers: Emergency use authorization for Paxlovid.(2021) U.S. FDA. <https://www.fda.gov/media/155050/download>. Accessed June 10, 2024
13. Heskin J, Pallett SJC, Mughal N, Davies GW, Moore LSP, Rayment M et al (2022) Caution required with use of ritonavir-boosted PF-07321332 in COVID-19 management. *Lancet* 399:21–22
14. Meyer C, Garzia A, Miller MW, Huggins DJ, Myers RW, Hoffmann HH et al (2025) Small-molecule inhibition of SARS-CoV-2 NSP14 RNA cap methyltransferase. *Nature* 637:1178–1185
15. Bouvet M, Imbert I, Subissi L, Gluais L, Canard B, Decroly E (2012) RNA 3'-end mismatch excision by the severe acute respiratory syndrome coronavirus nonstructural protein nsp10/nsp14 exoribonuclease complex. *Proc Natl Acad Sci USA* 109:9372–9377
16. Ogando NS, El Kazzi P, Zevenhoven-Dobbe JC, Bontes BW, Decombe A, Posthuma CC et al (2021) Structure-function analysis of the nsp14 N7-guanine methyltransferase reveals an essential role in Betacoronavirus replication. *Proc Natl Acad Sci USA* 118:e2108709118
17. Imprachin N, Yosaatmadja Y, Newman JA (2023) Crystal structures and fragment screening of SARS-CoV-2 NSP14 reveal details of exoribonuclease activation and mRNA capping and provide starting points for antiviral drug development. *Nucleic Acids Res* 51:475–487
18. Newman JA, Douangamath A, Yadzani S, Yosaatmadja Y, Aimon A, Brandao-Neto J et al (2021) Structure, mechanism and crystallographic fragment screening of the SARS-CoV-2 NSP13 helicase. *Nat Commun* 12:4848
19. Chen J, Zhou Y, Wei X, Xu X, Qin Z, Ong CP et al (2024) Development of pan-anti-SARS-CoV-2 agents through allosteric inhibition of nsp14/nsp10 complex. *ACS Infect Dis* 10:858–869
20. Yuan S, Wang R, Chan JF, Zhang AJ, Cheng T, Chik KK et al (2020) Metallo drug ranitidine bismuth citrate suppresses SARS-CoV-2 replication and relieves virus-associated pneumonia in Syrian hamsters. *Nat Microbiol* 5:1439–1448
21. Wei X, Chan CL, Zhou Y, Tang K, Chen J, Wang S et al (2024) Mechanistic insights into bismuth(III) inhibition of SARS-CoV-2 helicase. *Chem Sci* 15:10065–10072
22. Li H, Yuan S, Wei X, Sun H (2022) Metal-based strategies for the fight against COVID-19. *Chem Commun* 58:7466–7482
23. Wang R, Chan JF, Wang S, Li H, Zhao J, Ip TK et al (2022) Orally administered bismuth drug together with N-acetyl cysteine as a broad-spectrum anti-coronavirus cocktail therapy. *Chem Sci* 13:2238–2248
24. Rothan HA, Stone S, Natekar J, Kumari P, Arora K, Kumar M (2020) The FDA-approved gold drug auranofin inhibits novel coronavirus (SARS-COV-2) replication and attenuates inflammation in human cells. *Virology* 547:7–11
25. Marzo T, Messori L (2020) A role for metal-based drugs in fighting COVID-19 infection? The case of auranofin. *ACS Med Chem Lett* 11:1067–1068
26. Biji A, Khatun O, Swaraj S, Narayan R, Rajmani RS, Sardar R et al (2021) Identification of COVID-19 prognostic markers and therapeutic targets through meta-analysis and validation of Omics data from nasopharyngeal samples. *eBioMedicine* 70:103525
27. Gil-Moles M, Turck S, Basu U, Pettenuzzo A, Bhattacharya S, Rajan A et al (2021) Metallo drug profiling against SARS-CoV-2 target proteins identifies highly potent inhibitors of the S/ACE2 interaction and the papain-like protease PL(pro). *Chem Eur J* 27:17928–17940
28. Gil-Moles M, Basu U, Büssing R, Hoffmeister H, Türck S, Varchmin A et al (2020) Gold metallo drugs to target coronavirus proteins: Inhibitory effects on the Spike-ACE2 interaction and on PLpro protease activity by auranofin and gold organometallics. *Chem Eur J* 26:15140–15144
29. Sargsyan K, Lin C-C, Chen T, Grauffel C, Chen Y-P, Yang W-Z et al (2020) Multi-targeting of functional cysteines in multiple conserved SARS-CoV-2 domains by clinically safe Zn-ejectors. *Chem Sci* 11:9904–9909
30. Massai L, Grifagni D, De Santis AD, Geri A, Cantini F, Calderone V et al (2022) Gold-based metal drugs as inhibitors of coronavirus proteins: The inhibition of SARS-CoV-2 main protease by auranofin and its analogs. *Biomolecules* 12:1675
31. Shapiro DL, Masci JR (1996) Treatment of HIV associated psoriatic arthritis with oral gold. *J Rheumatol* 23:1818–1820
32. Langsjoen RM, Auguste AJ, Rossi SL, Roundy CM, Penate HN, Kastis M et al (2017) Host oxidative folding pathways offer novel anti-chikungunya virus drug targets with broad spectrum potential. *Antiviral Res* 143:246–251
33. Lin S, Chen H, Chen Z, Yang F, Ye F, Zheng Y et al (2021) Crystal structure of SARS-CoV-2 nsp10 bound to nsp14-ExoN domain reveals an exoribonuclease with both structural and functional integrity. *Nucleic Acids Res* 49:5382–5392
34. Ma Y, Wu L, Shaw N, Gao Y, Wang J, Sun Y et al (2015) Structural basis and functional analysis of the SARS coronavirus nsp14-nsp10 complex. *Proc Natl Acad Sci USA* 112:9436–9441
35. Greenfield NJ (2006) Using circular dichroism spectra to estimate protein secondary structure. *Nat Protoc* 1:2876–2890
36. Micsonai A, Bulyáki É, Kardos J (2021) BeStSel: From secondary structure analysis to protein fold prediction by circular dichroism spectroscopy. *Methods Mol Biol* 2199:175–189
37. Maio N, Raza MK, Li Y, Zhang DL, Bollinger JM Jr, Krebs C et al (2023) An iron-sulfur cluster in the zinc-binding domain of the SARS-CoV-2 helicase modulates its RNA-binding and -unwinding activities. *Proc Natl Acad Sci USA* 120:e2303860120
38. Zielonka J, Joseph J, Sikora A, Hardy M, Ouari O, Vasquez-Vivar J et al (2017) Mitochondria-targeted triphenylphosphonium-based compounds: Syntheses, mechanisms of action, and therapeutic and diagnostic applications. *Chem Rev* 117:10043–10120
39. Chiaverini L, Pratesi A, Cirri D, Nardinocchi A, Tolbatov I, Marone A et al (2022) Anti-Staphylococcal activity of the auranofin analogue bearing acetylcysteine in place of the thiosugar: An experimental and theoretical investigation. *Molecules* 27:2578
40. Kazimi SGT, Iqbal MS, Mulligan CC, Frank Shaw C, Iram F, Stelmack AR et al (2019) Ligand exchange/scrambling study of gold(I)-phosphine complexes in the solid phase by DESI-MS analysis. *J Am Soc Mass Spectrom* 30:2289–2296
41. Zheng Q, Borsley S, Nichol GS, Duarte F, Cockcroft SL (2019) The energetic significance of metallophilic interactions. *Angew Chem Int Ed Engl* 58:12617–12623
42. Sanchez-de-Diego C, Marmol I, Perez R, Gascon S, Rodriguez-Yoldi MJ, Cerrada E (2017) The anticancer effect related to disturbances in redox balance on Caco-2 cells caused by an alkynyl gold(I) complex. *J Inorg Biochem* 166:108–121
43. Yuan S, Chan JFW, Chik KKH, Chan CCY, Tsang JOL, Liang R et al (2020) Discovery of the FDA-approved drugs bexarotene, cetilistat, diiodohydroxyquinoline, and abiraterone as potential COVID-19 treatments with a robust two-tier screening system. *Pharmacol Res* 159:104960
44. Yuan S, Chan CC, Chik KK, Tsang JO, Liang R, Cao J et al (2020) Broad-spectrum host-based antivirals targeting the interferon and lipogenesis pathways as potential treatment options for the pandemic coronavirus disease 2019 (COVID-19). *Viruses* 12:628
45. Canal B, McClure AW, Curran JF, Wu M, Ulferts R, Weissmann F et al (2021) Identifying SARS-CoV-2 antiviral compounds by screening for small molecule inhibitors of nsp14/nsp10 exoribonuclease. *Biochem J* 478:2445–2464
46. Yuan S, Yin X, Meng X, Chan JF, Ye ZW, Riva L et al (2021) Clofazimine broadly inhibits coronaviruses including SARS-CoV-2. *Nature* 593:418–423

Publisher's Note Springer Nature remains neutral with regard to jurisdictional claims in published maps and institutional affiliations.

Authors and Affiliations

Jingxin Chen^{1,2} · Xueying Wei^{1,2} · Chun-Lung Chan¹ · Kaiming Tang² · Shuofeng Yuan² · Hongyan Li¹ · Hongzhe Sun¹

✉ Hongzhe Sun
hsun@hku.hk

² Department of Microbiology and State Key Laboratory of Emerging Infectious Diseases, The University of Hong Kong, Pokfulam Road, Hong Kong SAR, China

¹ Department of Chemistry and HKU-CAS Joint Laboratory of Metallomics on Health and Environment, The University of Hong Kong, Pokfulam Road, Hong Kong SAR, China